Production of primary mirror segments for the Giant Magellan Telescope

H. M. Martin[a], R. G. Allen[a], J. H. Burge[a,b], J. M. Davis[a], W. B. Davison[a], M. Johns[c], D. W. Kim[b], J. S. Kingsley[a], K. Law[a], R. D. Lutz[a], P. A. Strittmatter[a], P. Su[b], M. T. Tuell[a], S. C. West[a] and P. Zhou[b]

[a]Steward Observatory, University of Arizona, Tucson, AZ 85721, USA
[b]College of Optical Sciences, University of Arizona, Tucson, AZ 85721, USA
[c]GMTO Corporation, 251 South Lake Ave, Suite 300, Pasadena, CA 91101, USA

ABSTRACT

Segment production for the Giant Magellan Telescope is well underway, with the off-axis Segment 1 completed, off-axis Segments 2 and 3 already cast, and mold construction in progress for the casting of Segment 4, the center segment. All equipment and techniques required for segment fabrication and testing have been demonstrated in the manufacture of Segment 1. The equipment includes a 28 m test tower that incorporates four independent measurements of the segment's figure and geometry. The interferometric test uses a large asymmetric null corrector with three elements including a 3.75 m spherical mirror and a computer-generated hologram. For independent verification of the large-scale segment shape, we use a scanning pentaprism test that exploits the natural geometry of the telescope to focus collimated light to a point. The Software Configurable Optical Test System, loosely based on the Hartmann test, measures slope errors to sub-microradian accuracy at high resolution over the full aperture. An enhanced laser tracker system guides the figuring through grinding and initial polishing. All measurements agree within the expected uncertainties, including three independent measurements of radius of curvature that agree within 0.3 mm. Segment 1 was polished using a 1.2 m stressed lap for smoothing and large-scale figuring, and a set of smaller passive rigid-conformal laps on an orbital polisher for deterministic small-scale figuring. For the remaining segments, the Mirror Lab is building a smaller, orbital stressed lap to combine the smoothing capability with deterministic figuring.

Keywords: Giant Magellan Telescope, telescopes, optical fabrication, optical testing, off-axis, aspheres, active optics

1. INTRODUCTION

The GMT primary mirror consists of seven 8.4 m honeycomb mirrors that are being cast and polished at the Steward Observatory Mirror Lab. Each segment is similar to one of the primary mirrors of the Large Binocular Telescope and has the same advantages of high stiffness, low weight and short thermal time constant. For GMT, the 8.4 m segments guarantee a smooth wavefront over the largest subapertures possible, and minimize the number of optics to control. Since each primary mirror segment is matched to a 1.1 m segment of the secondary mirror, fine alignment and phasing can be done by moving the small, agile secondary segments, which are also the deformable mirrors for adaptive optics.[1],[2]

The first off-axis segment was completed in August 2012. Achieving this milestone retired the most significant technical risk for the GMT project, and completed the development of all equipment needed to make the full set of seven segments plus one spare. The Mirror Lab now has two 8.4 m machines for grinding and polishing, a 28 m test tower with four independent optical test systems installed in it, as well as tools and techniques for figuring the segments. The Lab continues to refine the equipment and techniques, but the essential pieces have been built and demonstrated.

Section 2 of this paper describes the status of segment production. Section 3 presents the results for Segment 1, including independent measurements of segment geometry and low-order aberrations, measurements that are critical to ensuring that all segments match in the telescope. Section 4 describes upgrades to the manufacturing equipment for Segments 2-8.

2. STATUS OF SEGMENT PRODUCTION

The six off-axis segments, plus one spare, have identical designs and will be interchanged as part of the coating cycle in the telescope. The first of these was completed in August 2012. Section 3 reports the quality of Segment 1 and the full

set of measurements that were made. Segments 2 and 3, also off-axis segments, have been cast and are in early stages of fabrication. Both castings produced mirror blanks of excellent quality. Segment 2 was cast in January 2012[3] and had its rear surface machined and polished in preparation for bonding the 165 loadspreaders that are the interface between the mirror and its support system in the telescope. The front surface will be machined in late 2014. Segment 3 was cast in August 2013 and is being prepared to have its rear surface machined in early 2015.

Segment 4 will be the center segment, which will make it possible for the project to proceed with an initial commissioning with a close-packed array of four segments. The mold for Segment 4 is being assembled in preparation for a casting scheduled for March 2015. We have completed the first part of an engineering study for the center segment, finalizing the design of the segment and its support system. The second part of the study will include conceptual design of the modifications to the measuring equipment, which will be reconfigured for the symmetric segment. We have purchased the Ohara E6 glass for off-axis Segment 5, which will be cast in 2016.

Due to prior commitments at the Mirror Lab, Segment 2 follows two other mirrors through the production queue. These are the combined primary and tertiary mirrors of the LSST and a primary mirror for a 6.5 m telescope. Following these, the only mirrors in the queue are the GMT segments. As of May 2014, the LSST mirror is on the Large Polishing Machine and the 6.5 m mirror is having its front surface machined on the Large Optical Generator, both in the Mirror Lab's polishing lab. GMT Segment 2 is in the adjacent integration lab having its loadspreaders bonded to the rear surface, and Segment 3 is in the casting lab having the ceramic fiber mold removed from the honeycomb mirror. Figure 1 shows GMT Segments 2 and 3.

Figure 1. Left photo: GMT Segment 2 with its rear surface up in preparation for bonding of loadspreaders. A laser tracker at the center of the mirror is used to set the locations of the loadspreaders. Segment 1, with a protective cover for storage, is to the left of Segment 2. Right photo: Segment 3 being moved from the furnace to a handling ring prior to removal of the ceramic fiber mold. The mirror is lifted by a steel frame with 36 disks bonded to the mirror surface with compliant silicone adhesive. Photos by Ray Bertram.

3. RESULTS FOR SEGMENT 1

The basic figure results for Segment 1 were given in Ref. [3]. Following that publication we completed the acceptance tests, including independent measurements of the segment's radius of curvature R, off-axis distance Δx, clocking θ (rotation around the center of the segment), and certain low-order aberrations. The segments must match in radius of curvature accurately enough that the active-optics correction at the telescope (described below) can bring them to essentially the same radius. Errors in Δx and θ must be less than the available travel for positioning the segment relative to the telescope structure, specified as 2 mm for Δx (with a goal of 1 mm) and 50 arcseconds for θ. We refer to the combination of R, Δx and θ as the segment geometry.

3.1 Methods of measurement

The methods of measuring the segments have been described in a number of papers, but we will summarize them here as background for a discussion of the results for Segment 1. We use four independent test systems to measure the GMT segments:

1. principal test, a full-aperture interferometric test using a large asymmetric null corrector;[4],[5]

2. scanning pentaprism test, which measures slope errors across any diameter of the segment;[6],[7],[8]

3. Laser Tracker Plus (LT+), a survey of the surface with an enhanced laser tracker;[9],[10]

4. Software Configurable Optical Test System (SCOTS), a full-aperture slope test.[11],[12]

Our analysis shows that the principal test satisfies all essential requirements for accuracy, but we need independent verification of certain critical parameters. The principal test uses a large and complex null corrector whose accuracy depends on precise alignment measurements. For symmetric mirrors such as the primary mirrors for the MMT, Magellan telescopes and LBT, it was possible to verify the accuracy of the much smaller null corrector by using it to measure a small (~20 cm) computer-generated hologram that mimicked a perfect primary mirror. No such test of the GMT null corrector is possible, so we perform the independent verification by measuring the segment with the scanning pentaprism test and LT+ (for large-scale accuracy) and SCOTS (for small-scale accuracy).

Figure 2 shows the layout of the principal test. The null corrector includes a 3.75 m spherical mirror, a smaller mirror and a computer-generated hologram. Elements of the null corrector are spread over a distance of 9 m and the separation between the 3.75 m mirror and the GMT segment is 24 m. We measure the larger dimensions to an accuracy of about 100 microns with a laser tracker, but the resulting uncertainty in alignment causes significant uncertainty in low-order aberrations, especially focus, astigmatism and coma. The 2σ uncertainties are about 1100 nm rms in focus, 300 nm rms in each component of astigmatism, and 60 nm rms in each component of coma. These uncertainties include the effects of support force errors and temperature gradients in the segment, as well as misalignment of the test system. Errors in segment geometry are equivalent to low-order aberrations, so we have corresponding uncertainties in R, Δx and θ.
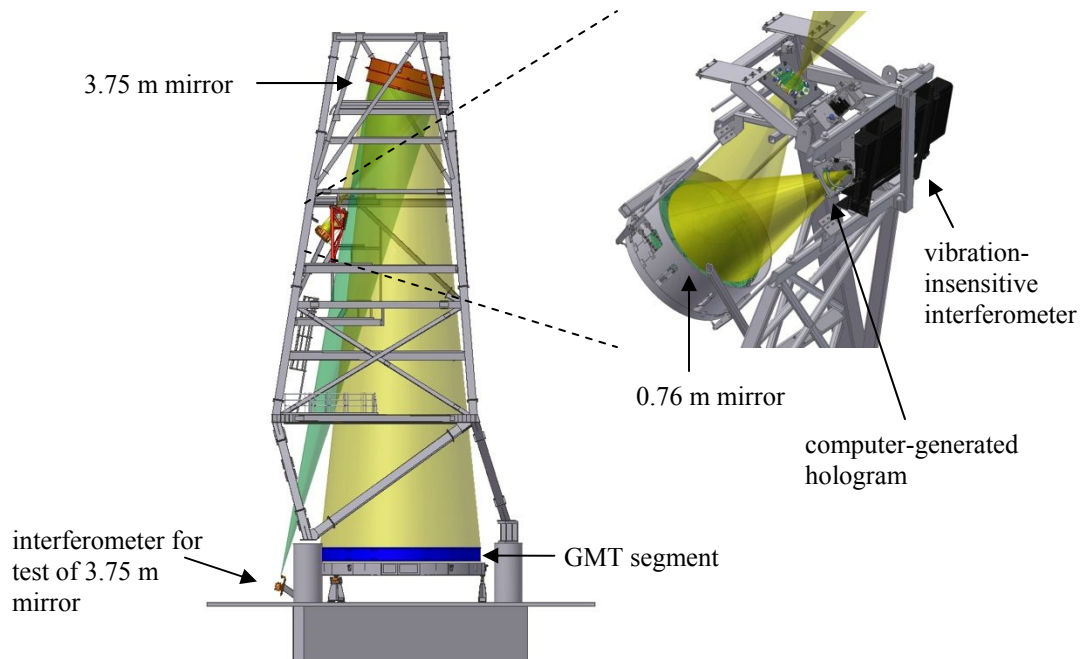

Figure 2. Model of the principal optical test for the GMT off-axis segments, in the 28 m test tower. At right is a blow-up of the interferometer and first two elements of the null corrector. Gold light cones represent the measurement of the GMT segment, while the aqua cone in the full model at left represents a simultaneous measurement of the 3.75 m fold sphere.

These uncertainties in low-order aberrations, while large compared with acceptable wavefront errors, are well within the range of correction using active optics at the telescope, as discussed below. Viewed as errors in prescription or alignment, they are similar to the tolerances for symmetric mirrors, despite the much larger and more complex null corrector. The uncertainty in focus corresponds to an uncertainty in radius of curvature $\Delta R = 0.6$ mm, tighter than the typical tolerance for a symmetric mirror where there is no requirement to match in radius. (The pentaprism test and LT+ measure the radius to about 0.4 mm.) The uncertainties in astigmatism and coma correspond to translations of about 1 mm, a typical centration tolerance for a symmetric mirror, and to clocking of about 15 arcseconds.

The analysis of errors in alignment of the test optics is based on the active optics procedure that will be carried out after the segment is installed in the telescope and its wavefront errors are measured with the wavefront sensor. The segment's position within the parent surface will be adjusted to reduce aberrations that depend strongly on position. Table 1 lists the sensitivity of those aberrations to off-axis distance and clocking. Once the segment is moved to the optimum position, the support forces will be adjusted to bend out the residual wavefront error. In order to limit the magnitude of correction forces, the forces are applied as a limited number of bending modes. Table 2 lists the magnitudes of support forces required to bend out representative amounts of five aberrations, along with the residual surface error after bending. The magnitudes before correction in Table 2 represent roughly the 2σ uncertainties in the principal test.

Table 1. Sensitivity of low-order aberrations to off-axis distance and clocking. Clocking by 50 arcsec causes a point at the edge to move by 1 mm.

aberration	rms surface error (nm)	
	1 mm change in off-axis distance	50" rotation
focus	810	
astigmatism	510	1240
coma	34	160

Table 2. Correction forces and residual surface errors for some low-order aberrations, defined as Zernike polynomials. The correction uses 27 bending modes.

aberration	focus	astigmatism	coma	trefoil	spherical aberration
magnitude before correction (nm rms)	1100	300	60	30	15
rms force (N)	60	6	9	2	6
residual error (nm rms)	32	3	8	1	4

Focus is the only aberration that should not be bent out, because of the large correction forces and residual error. The shift in off-axis distance is therefore optimized to correct the focus error, leaving mostly astigmatism and coma to be bent out. More precisely, the algorithm adjusts the segment's position to minimize the rms correction force that will be required to correct the residual aberrations after the position adjustment. Note that this active-optics correction completely eliminates the low-order aberrations, leaving higher-order residual errors. For focus, this means eliminating any error in radius of curvature, making all segments match precisely in radius. In practice, the accuracy of these aberrations will be limited by the wavefront measurements at the telescope and not by the quality of the segments.

In order to determine the impact of misalignment of the test, we simulate the active-optics correction. For each misalignment, say a tilt of the 3.75 m mirror, we compute the resulting wavefront error using optical design software. We optimize the segment's position in the telescope, and correct the remaining errors by bending the segment, i. e. by adding certain bending modes computed from the finite-element model. We record the shift in off-axis distance and

clocking angle, the rms force over the 165 actuators, and the rms residual surface error. We repeat this process for all components of alignment error, and add the results in quadrature. Ref. [5] contains a full list of misalignments and their impacts. The net result is 2σ uncertainties of 1.2 mm in off-axis distance, 7 arcseconds in clocking, 14 N rms correction force, and 16 nm rms residual surface error. These are all acceptable uncertainties.

The analysis outlined above assumes that the principal test is aligned to the expected accuracy. We require independent measurements to guard against the possibility of a mistake in assembling the principal test. We are most concerned about verifying the segment geometry and low-order aberrations because they are the parameters most sensitive to alignment of the principal test. With redundant measurements of all critical parameters, we have very high confidence that each segment is made to the right prescription and will deliver a good wavefront at the telescope.

The scanning pentaprism test uses the telescope's natural geometry to focus a narrow collimated beam onto a detector at the telescope's prime focus. A pentaprism on a rail scans the beam across the segment's diameter; motion of the focused spot is used to determine the slope errors on the segment surface. A second, stationary beam is used to correct for motion of the segment, the detector, and the pentaprism rail. The differential measurement using both focused spots determines the segment's slope errors to an accuracy of about 0.5 microrad rms surface. By scanning across five diameters and fitting Zernike polynomials to the measured slopes, we can determine the polynomials through r^3, plus spherical aberration, to an accuracy similar to that of the principal test.

Laser Tracker Plus is a scan of about 250 points at roughly equal spacing across the surface. The tracker's sphere-mounted retroreflector is moved by an air-bearing puck across the surface and set in contact with the surface at each sample point. The laser tracker is located about 22 m above the segment, as close to the center of curvature as we can reach, in order to make its line of sight almost normal to the surface and thereby reduce the coupling between angles measured by the tracker and surface normal displacement on the segment. (The tracker measures line-of-sight displacements much more accurately than lateral displacements.) With this favorable geometry, and a custom calibration of the angle measurements, we can measure surface displacement to about 1 micron rms accuracy. We monitor relative motion between the segment and the tracker with a separate set of distance-measuring interferometers, and correct for it. LT+ is essential in the early stages of fabrication, before we have a specular surface for interferometric measurements. Because of the tracker's high accuracy in absolute distance and ~1 micron rms surface accuracy, LT+ measures the segment's radius of curvature to high accuracy, and measures astigmatism to a useful accuracy.

During all measurements, we monitor the 165 support forces, and the glass temperature at 36 points on the underside of the front facesheet and an equal number on the back plate. We compensate for the resulting figure changes based on finite-element models. The largest compensations are astigmatism due to force errors and the change in focus due to the average temperature difference between front and back of the mirror. A 0.1 K temperature difference causes 1.4 microns rms focus error, equivalent to 0.8 mm in R. A ventilation system reduces the temperature difference below 0.02 K in most cases, and the differential measurements are good to about 0.01 K or 0.08 mm in R. By studying the correlation between predicted and measured figure changes, we determined that both force and temperature compensations improve the measurement accuracy but have significant uncertainties. We include an uncertainty equal to half the compensation in the estimated uncertainty of every test.

For the principal test and pentaprism test, we also compensate for small misalignments of the 3.75 m mirror, the pentaprism rail and detector, and the GMT segment; their alignment accuracies are limited by positioning resolution rather than measurement accuracy. We calculated the sensitivities of different aberrations to misalignments by perturbing the optical design, and verified them experimentally.

3.2 Agreement among the tests

The principal test, pentaprism test, and LT+ measure the absolute shape of the GMT segments to high accuracy. All three tests measure focus to $1\text{-}1.5\times10^{-5}$ of the segment's 232 mm sag, and measure astigmatism to $1\text{-}2.5\times10^{-4}$ of its 13 mm p-v astigmatism. Even the least accurate measurements of these aberrations guarantee that the segment can be corrected with active optics to give excellent performance at the telescope. The reason for redundant tests is to minimize the likelihood that a mistake in one of the tests could compromise the performance.

Table 3 lists the coefficients of 8 Zernike polynomials as determined by the principal test, pentaprism test and LT+. The estimated 2σ uncertainties are also listed. For LT+, we only list uncertainties for focus and astigmatism, because LT+ is not expected to be a meaningful verification test for higher-order aberrations. Table 3 shows that all meaningful measurements of aberrations through spherical agree within the 2σ uncertainties.

Table 3. Zernike polynomial coefficients for low-order aberrations measured with the principal test, pentaprism test and LT+. The polynomials are normalized so the absolute value of the coefficient equals the rms surface error in nm. The uncertainties are 2σ limits.

aberration	principal test		pentaprism test		LT+	
	measured	uncertainty	measured	uncertainty	measured	uncertainty
focus	-135	1100	-462	720	4	690
astigmatism 0°	-467	270	-346	680	-245	690
astigmatism 45°	-224	310	-550	670	-460	690
coma 0°	-123	64	-32	100	-47	
coma 90°	28	49	-23	120	-208	
trefoil 0°	36	32	19	230	170	
trefoil 30°	111	27	-19	230	131	
spherical	-42	15	-50	56	-99	

The initial pentaprism test during the acceptance testing gave a value of -98 nm for spherical aberration. Using the 2σ uncertainties, this was marginally consistent with the principal test's value of -42 nm, but we expected better agreement. The segment had been figured on the basis of the principal test, and the large-scale figure errors including spherical aberration were easily corrected with active optics. The pentaprism's larger value of spherical aberration would have been correctable but would have required larger forces and left larger residual errors. Because of a coupling between bending of focus and spherical aberration, the active correction required a larger shift in off-axis distance (1.1 mm vs 0.2 mm) in order to give a more favorable focus error before bending.

We investigated both measurements, looking for an error in spherical aberration, and eventually found an unanticipated effect in the pentaprism system. The detector at the prime focus was a Kodak Kai-16000 image sensor, with a micro-lens array in front of the detector. In lab experiments, we found that the micro-lenses displaced the incident light as a function of angle of incidence (AOI). As the beam is scanned across the segment diameter, its AOI at the detector varies over ±14°. We found a cubic dependence of apparent spot position as a function of AOI, with a maximum spot displacement of 12 microns. Because the pentaprism test measures slope error, the cubic variation is the signature of spherical aberration on the segment. The magnitude of the lens effect corresponds to 48 nm of spherical aberration in the segment, nearly matching the discrepancy between the principal test and pentaprism test. We performed the same test with a detector that had no micro-lens array and found no cubic dependence on AOI. We used the results of the lab experiment to correct the GMT pentaprism data, obtaining the aberrations listed in Table 3.

With the discrepancy in spherical aberration resolved, all three tests agree within expected uncertainties for all aberrations through spherical. This validates the large-scale accuracy of the principal test. Combining the three tests gives a better estimate of the aberrations, as well as the radius of curvature, off-axis distance and clocking.

3.3 Results of measurements

Segment 1 was completed in August 2012. Following a set of acceptance tests, whose results are reported here, the segment was accepted by the GMTO Corporation. The surface is accurate to 18 nm rms after the simulated active-optics correction using 27 bending modes. Three independent measurements of the absolute shape of the mirror agree well within their expected uncertainties for focus, astigmatism, coma, trefoil and spherical aberration. The agreement for focus, astigmatism and coma establishes that the segment has the correct geometry.

As described in Ref. [3], the principal test lost some data in the outer 10 cm of the aperture due to a combination of high slope errors and limited spatial resolution (caused in part by image distortion from the asymmetric null corrector). The final map used to quantify the performance of the segment combines data from the principal test and SCOTS, with SCOTS data stitched to the principal test map to fill in the outer 10 cm. The active optics correction is simulated using different numbers of bending modes. Using more bending modes improves the large-scale figure but has almost no

impact on the small-scale structure. Figure 3 shows the stitched maps after active correction using 20, 27 and 46 bending modes. (Each successive correction includes one more axisymmetric mode.)
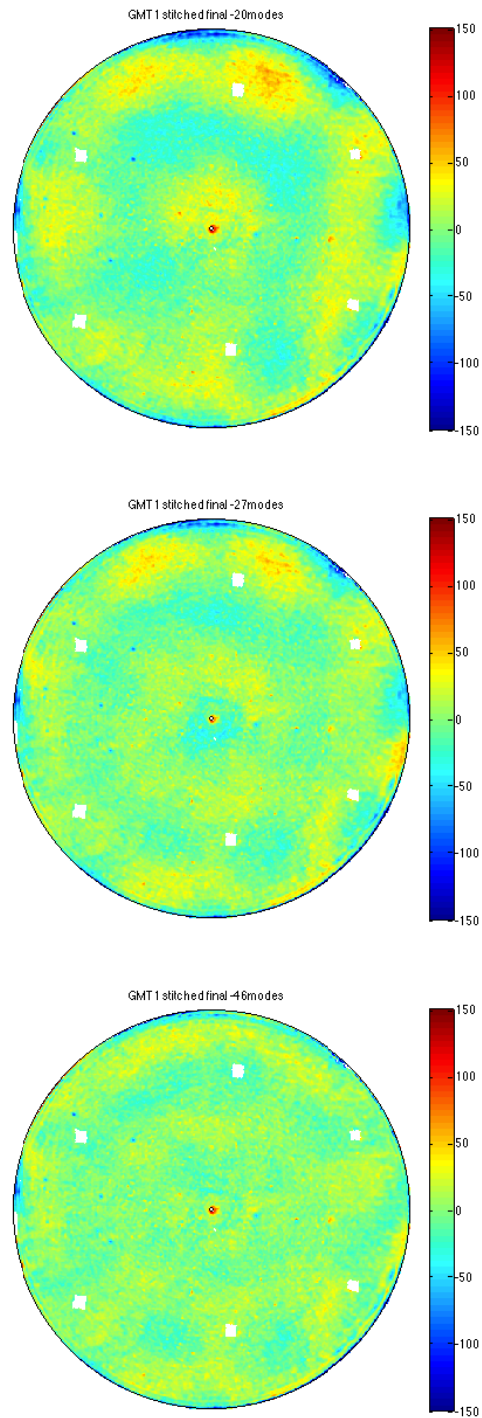

Figure 3. Figure of GMT Segment 1 after simulated active-optics correction. The correction uses 20 bending modes (top), 27 modes (middle) and 46 modes (bottom). The plots cover the full optical surface with a diameter of 8.405 m and inner diameter of 6 cm (a drain hole to facilitate grinding and polishing). Color bar is in nm of surface error.

Table 4 summarizes the results for the maps in Figure 3. The table lists the displacement of the segment (change in off-axis distance and clocking) and the correction forces for the active-optics correction, and the rms surface error after the correction. The conservative active-optics correction using only 20 bending modes gives an excellent mirror surface with 22 nm rms surface error; with a more aggressive correction using 46 modes the rms error is reduced to 15 nm.

Table 4. Results of simulated active-optics correction for the maps in Figure 3. The rms surface error is computed over the clear aperture with a diameter of 8.365 m.

number of bending modes	20	27	46
change in off-axis distance (mm)	0.29	0.24	0.24
clocking (arcsec)	3	0	1
rms force (N)	17	21	27
rms surface error (nm)	22	18	15

The active-optics correction converts uncertainties in aberrations to uncertainties in off-axis distance, clocking, rms force and rms surface error. Table 5 includes these uncertainties to show that the maximum likely value of each parameter is within its tolerance. As discussed earlier, the active-optics correction includes correction of focus, which is equivalent to radius of curvature. Therefore Table 5 does not include an error in radius, but the rms force and rms surface error include the correction of radius. There is no tolerance on rms surface error; the structure function figure specification limits the allowed surface error after active correction. The residual errors are on medium spatial scales of 1-2 m, where the specification allows errors of 50-70 nm rms surface.

Table 5. Results for the 27-mode correction, including 2σ uncertainties in the principal test. The maximum likely value of each parameter is the upper limit for 95% confidence.

parameter	value from principal test	uncertainty	maximum likely value	tolerance
change in off-axis distance (mm)	0.24	1.2	±1.2	2.0
clocking (arcsec)	0	13	±13	50
rms force (N)	21	14	25	42
rms surface error (nm)	19	16	25	

There is also a specification to measure the radius of curvature, before active-optics correction, to an accuracy of 0.5 mm. (This is not needed to guarantee excellent performance in the telescope; the preceding results show that the error in R can be eliminated with active optics.) The principal test, pentaprism test, and LT+ all measure focus, which is equivalent to the error in R. The measured values of focus in Table 3 may be converted to radius error. The measured values and their uncertainties are used to determine a best estimate and uncertainty for the uncorrected radius of curvature. Table 6 lists the results and shows that the error in radius of curvature, before active correction, is 0.12 mm ± 0.40 mm.

Table 6. Measurements of radius of curvature for the three tests, in mm, relative to the nominal value of 36 m. The uncertainties for the individual tests are 2σ values, and the uncertainty for the weighted average is a conservative limit for 95% confidence.

method	radius error	uncertainty
principal test	0.08	0.62
pentaprism test	0.26	0.41
LT+	0.00	0.39
weighted average	0.12	0.40

Figure 4 shows the structure functions over the 8.365 m clear aperture for the maps of Figure 3. The measured structure function exceeds the specification for separations between 3 and 8 cm, but by less than 10%. Figure 5 shows the structure function over several aperture sizes, using the map corrected with 27 bending modes. The structure function improves rapidly as the aperture is decreased, because the errors are concentrated at the edge. A reduction from the 8.365 m clear aperture to an 8.3 m aperture improves the accuracy substantially, and gives a structure function within the specification at all separations. The project determined that Segment 1 will produce excellent images despite slightly failing to meet the structure function specification over the clear aperture, and that further work on it is not an effective use of resources. The Mirror Lab continues to develop the fabrication and testing techniques, and expects to meet all specifications for the remaining segments. We describe in Section 4 a new orbital stressed lap that is expected to provide better control of the figure near the edge.
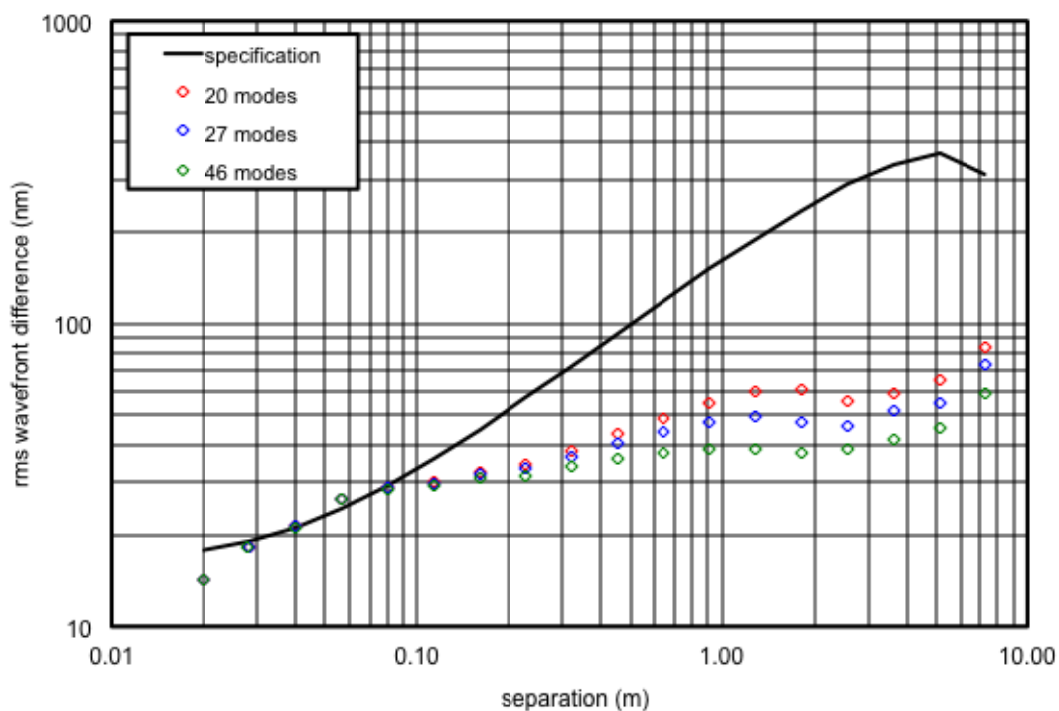

Figure 4. Structure functions over the 8.365 m clear aperture for the maps in Figure 3.
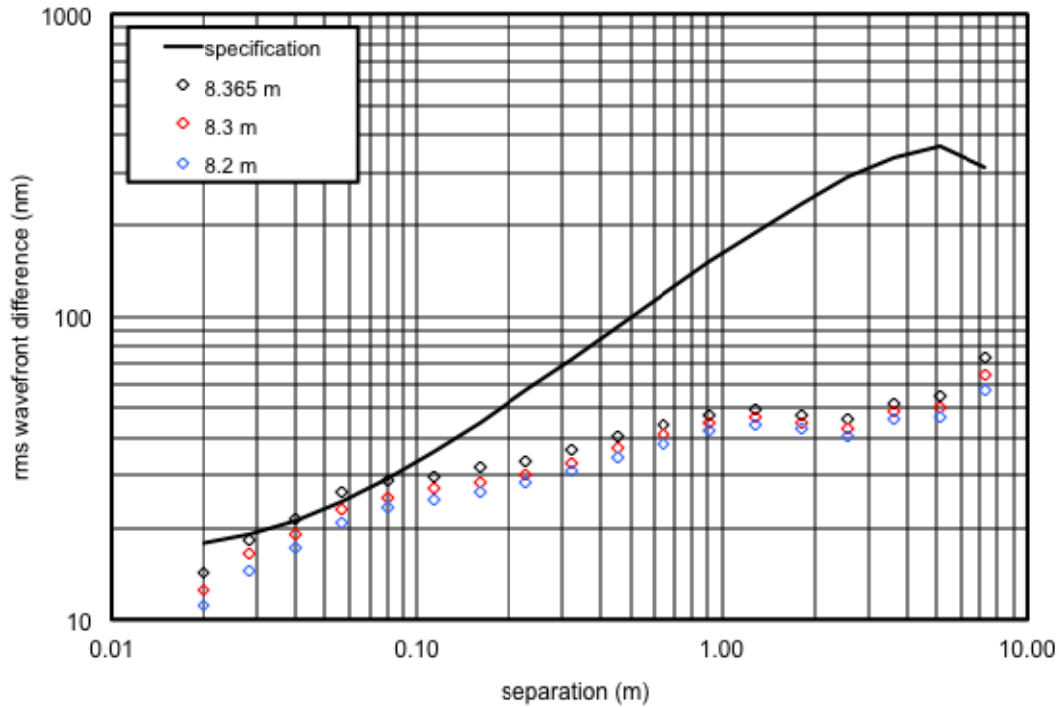
Figure 5. Structure functions over different apertures for the map corrected with 27 bending modes.

Finally, Figure 6 shows point-spread functions and encircled energy diagrams computed from the map with the 27-mode correction. Results are shown for Segment 1 and for a perfect mirror, in perfect seeing and in exceptionally good 0.2 arcsec seeing. Table 7 lists, for each case, the diameter containing 80% of the light and the fraction of light in a 1 arcsec diameter circle. In perfect seeing, Segment 1 would focus 80% of the light in 0.072 arcsec, less than half the diameter allowed by the telescope error budget and close to the goal of 0.054 arcsec. In 0.2 arcsec seeing, Segment 1 would cause only a 12% degradation of the image from a perfect mirror.

Table 7. Diameter containing 80% of the light, and fraction of light contained in a 1 arcsec diameter circle, for the point-spread functions shown in Figure 6.

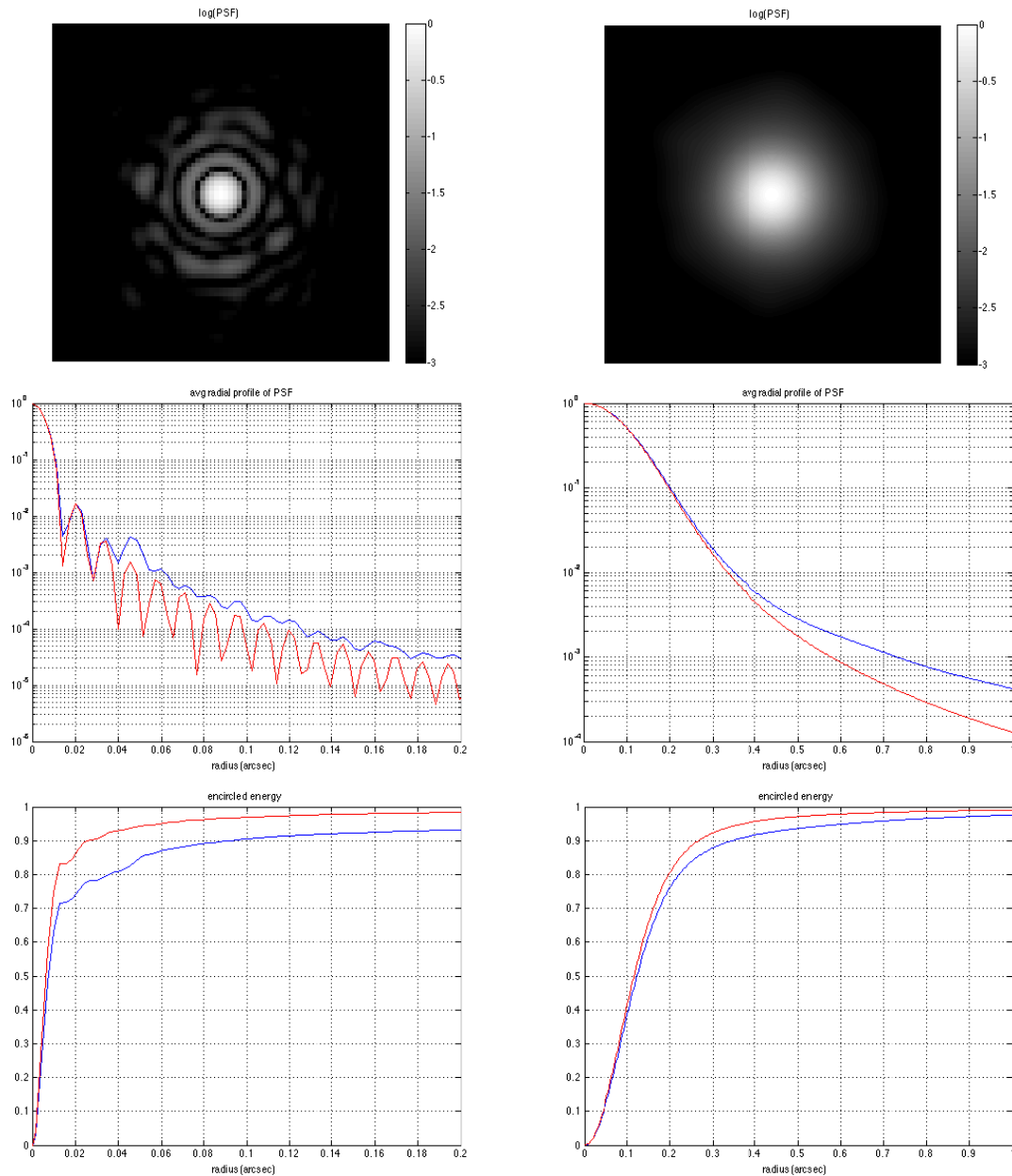|	perfect seeing		0.2 arcsec seeing	
	θ_{80} (arcsec)	fraction in 1"	θ_{80} (arcsec)	fraction in 1"
GMT Segment 1	0.072	0.958	0.441	0.936
perfect mirror	0.024	0.994	0.393	0.971

Figure 6. Point-spread function and encircled energy at $\lambda = 500$ nm for the map corrected using 27 bending modes. Three plots at left are for Segment 1 alone without seeing. Three plots at right are for Segment 1 with 0.2 arcsec seeing. The 2-D PSFs and blue curves are for the actual mirror, and the red curves are for a perfect mirror. The 2-D PSFs have logarithmic intensity scales and show a 0.2 arcsec square for Segment 1 with no seeing, and a 2 arcsec square for Segment 1 with 0.2 arcsec seeing.

4. PREPARATIONS FOR FUTURE SEGMENTS

We are making a number of minor upgrades to the optical test equipment, and some improvements in software for data acquisition and processing, before we polish and measure Segment 2. We are making one significant upgrade to the fabrication capabilities. We polished Segment 1 with a 1.2 m stressed lap and a set of small passive rigid-conformal (RC) laps.[13],[14] The stressed lap was used for large-scale figuring and smoothing of small-scale structure. It has some smoothing capability because it is a stiff lap that is bent actively to follow the varying curvature of the aspheric mirror

Proc. of SPIE Vol. 9151 91510J-11

surface. The RC laps were used with an orbital polisher in a traditional computer-controlled polishing mode, where the dwell is varied to control removal as a function of position on the mirror. This method did an excellent job controlling mid-scale structure over almost the full surface, but provided little smoothing of small-scale structure. Both methods had limitations at the edge of Segment 1. The stressed lap is too large to do any figuring of the outer 20 cm, and its ability to smooth or maintain an accurate figure on the off-axis segment was not as good as we have experienced with symmetric mirrors. The RC laps are too compliant to smooth, and their removal footprints cannot be centered close to the edge without the lap tipping over at the extreme point in its orbit. The result of these limitations was figure errors that are highly concentrated at the edge.

To improve the figuring capability, especially at the edge, we plan to combine the smoothing capability of the stressed lap with the deterministic figuring of the orbital polisher. We have designed a smaller, 60 cm stressed lap, shown in Figure 7, to be used with an orbital polisher. Its basic design and operation are similar to the 1.2 m stressed lap that we used for Segment 1 and other mirrors. The design has evolved through an orbital stressed lap, also 60 cm diameter, in use at the University of Arizona College of Optical Sciences. The newest lap is designed specifically for GMT primary mirror segments, which minimizes compromises in the design. A 60 cm lap has to bend by a modest 200 microns p-v as it moves across a GMT segment, so we can use a stiff plate (good for smoothing) and small, lightweight actuators to bend it. The mass and the height of the center of gravity have been minimized in order to make the lap stable against tilt, reducing unwanted pressure gradients.
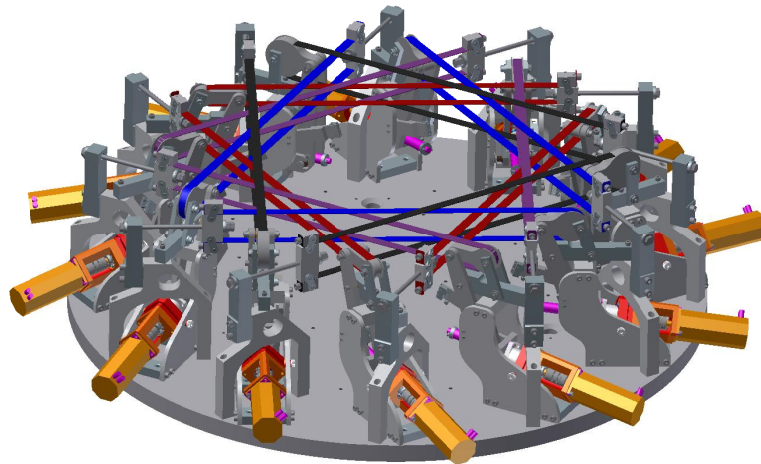

Figure 7. Model of a small stressed lap that will be used with an orbital polisher for the remaining GMT segments. It consists of an aluminum plate, 25 mm thick, with 12 bending actuators to control its shape. Not shown in the drawing are 3 lifting actuators that act through a load-spreader to control the polishing force and moments. The polishing surface has a diameter of 60 cm; the plate is somewhat larger in order to keep the print-through of the benders outside the polishing area.

We can achieve the most accurate bending with a flat plate, as opposed to a shell that matches the mirror's average curvature. The sag of the mirror across the 1.2 m stressed lap is 5 mm; such a large variation in pitch thickness would cause a large variation in polishing pressure, so the lap has a layer of nylon between the aluminum and the pitch to make up the sag. This nylon layer has unwanted effects on stiffness and shape control. For a 60 cm lap, the sag of the mirror surface is only 1.2 mm, probably small enough that it can be taken with pitch. The initial plan is to use a flat plate faced with pitch, with no intermediate layer.

The orbiting motion is key to the expected improvement in control of the mirror surface. Its removal footprint has a width roughly equal to the lap diameter and tapers to zero. This is much better suited to figuring than the large rotating stressed lap, whose footprint has an abrupt edge. The orbital stressed lap will be used like the RC laps, with high dynamic range of removal through variable dwell. This method provides very efficient control of figure errors down to about half the lap diameter, or 30 cm. The stressed lap is stiff enough to remove small-scale structure passively, and to reduce pressure variations due to distortion of the lap when it extends over the edge of the mirror. We will also use the benders to further reduce the lap distortion at the edge of the mirror.

For a rotating stressed lap, the greatest shape change and the highest demand on its benders come from matching the astigmatic component of the mirror surface as the lap rotates. The second highest demand comes from the varying distance between the lap and the mirror center (for an off-axis segment, the center of the parent). The orbital lap will rotate much more slowly, and generally moves much more slowly relative to the mirror center, so the benders require much lower bandwidth. More importantly, the slow variation in lap shape allows pitch flow to take up the residual misfit due to imperfect bending, leading to more accurate shape control and a consistent removal footprint.

5. CONCLUSION

The Mirror Lab is making good progress in production of segments for the GMT primary mirror. The first off-axis segment was finished with an excellent figure, validating the manufacturing process and retiring the most significant technical risk for the project. Three independent measurements of the segment's geometry and low-order aberrations agree within their uncertainties. This gives very high confidence that Segment 1, and all segments, will produce excellent images for the GMT.

The next two off-axis segments have been cast and are of excellent quality. We have completed work on the rear surface of Segment 2 and will machine the front surface in late 2014. Mold construction is underway for the casting of Segment 4, the center segment, in 2015.

The Mirror Lab continues to refine the tools and methods that we use to make and measure the GMT segments. We are developing a new orbital stressed lap that will combine deterministic figuring and smoothing capabilities, leading to more accurate segments and more efficient production.

ACKNOWLEDGEMENTS

REFERENCES

[1]   M. Johns, P. J. McCarthy, K. Raybould, A. Bouchez, A. Farahani, J. M. Filgueira, G. H. Jacoby, S. A. Shectman and M. Sheehan, "Giant Magellan Telescope: overview ", *Ground-based and Airborne Telescopes IV*, Proc. SPIE 8444, 84441H-1 (2012).

[2]   M. Johns, C. Hull, G. Muller, B. Irarrazaval, A. Bouchez, T. Chylek, C. Smith, A. Wadhavkar, B. Bigelow, S. Gunnels, B. McLeod and C. Buleri, "Design of the Giant Magellan Telescope", *Ground-based and Airborne Telescopes V*, Proc. SPIE 9145, paper 9145-50 (2014).

[3]   H. M. Martin, R. G. Allen, J. H. Burge, D. W. Kim, J. S. Kingsley, K. Law, R. D. Lutz, P. A. Strittmatter, P. Su, M. T. Tuell, S. C. West and P. Zhou, "Production of 8.4 m segments for the Giant Magellan Telescope", *Modern Technologies in Space- and Ground-based Telescopes and Instrumentation II*, Proc. SPIE 8450, 84502D-1 (2012).

[4]   J. H. Burge, W. Davison, H. M. Martin and C. Zhao, "Development of surface metrology for the Giant Magellan Telescope primary mirror", *Advanced Optical and Mechanical Technologies in Telescopes and Instrumentation*, Proc. SPIE 7018, 701814 (2008).

[5]   S. C. West, J. H. Burge, B. Cuerden, W. B. Davison, J. Hagen, H. M. Martin, M. T. Tuell and C. Zhao, "Alignment and use of the optical test for the 8.4m off-axis primary mirrors of the Giant Magellan Telescope", *Modern Technologies in Space- and Ground-based Telescopes and Instrumentation*, Proc. SPIE 7739, 77390N (2010).

[6]   P. Su, J. H. Burge, B. Cuerden and H. M. Martin, "Scanning pentaprism measurements of off-axis aspherics", *Advanced Optical and Mechanical Technologies in Telescopes and Instrumentation*, Proc. SPIE 7018, 70183T (2008).

[7]   P. Su, J. H. Burge, B. Cuerden, R. G. Allen and H. M. Martin, "Scanning pentaprism measurements of off-axis aspherics II," *Optical Manufacturing and Testing VIII*, Proc. SPIE 7426, 74260Y (2009).

[8]   R. G. Allen, J. H. Burge, P. Su and H. M. Martin, "Scanning pentaprism test for the GMT 8.4 m off-axis segments", *Modern Technologies in Space- and Ground-based Telescopes and Instrumentation*, Proc. SPIE 7739, 773911 (2010).

[9]   T. Zobrist, J. H. Burge, W. Davison and H. M. Martin, "Measurement of large optical surfaces with a laser tracker", *Advanced Optical and Mechanical Technologies in Telescopes and Instrumentation*, Proc. SPIE 7018, 70183U (2008).

[10]   T. L. Zobrist, J. H. Burge and H. M. Martin, "Accuracy of laser tracker measurements of the GMT 8.4 m off-axis mirror segments", *Modern Technologies in Space- and Ground-based Telescopes and Instrumentation*, Proc. SPIE 7739 (2010).

[11]   P. Su, R. E. Parks, L. Wang, R. Angel and J. H. Burge, "Software configurable optical test system: a computerized reverse Hartmann test," *Applied Optics*, Vol 49, Issue 23, pp 4404-4412 (2010).

[12]   P. Su, S. Wang, M. Khreishi, Y. Wang, T. Su, R. E. Parks, P. Zhou, M. Rascon, T. Zobrist, H. Martin and J. H. Burge, "SCOTS: A reverse Hartmann test with high dynamic range for Giant Magellan Telescope primary mirror segments", *Modern Technologies in Space- and Ground-based Telescopes and Instrumentation II*, Proc. SPIE 8450, 84500W-1 (2012).

[13]   D. W. Kim and J. H. Burge, "Rigid conformal polishing tool using non-linear visco-elastic effect", Opt. Express **18**, 2242-2257 (2010).

[14]   D. W. Kim, H. M. Martin and J. H. Burge, "Calibration and optimization of computer-controlled optical surfacing for large optics", *Optical Manufacturing and Testing IX*, Proc. SPIE 8126, 812615 (2011).